Chapter 7
Application Oriented Design of a Prototype Vibration Transducer

7.1 Introduction

Chapter 4 confirmed important results from the optimization approach in Chap. 3: Regardless of the considered coupling architecture there are dimensions for magnet, coil and (if existent) back iron components which result in a maximum output performance. Because there are separate optima for the output power and output voltage every electromagnetic vibration transducer can be designed either as a voltage– or a power source. Moreover there are architectures which inherently have a better output performance. These architectures should be preferred whenever possible. However, because different design constraints will apply even these architectures must be optimized for each application. Therefore, the optimization procedure developed provides a tool for the development of application oriented electromagnetic vibration transducers. To demonstrate the benefit of the optimization approach in the design process this chapter outlines the development of a prototype vibration transducer based on architecture A II. This architecture was chosen because of the simple assembly and the good voltage generation capability. However a basic drawback of this architecture is that the magnetic field is not channeled with back iron part. Hence the oscillator is sensitive against nonlinear forces generated by ferromagnetic components in the environment. Moreover, eddy currents will take place in metal components that are close to the generator reducing its power output.

The chapter is divided into five further sections. Section 7.2 introduces the basis for the development. The intended operation environment of the vibration transducer is the engine compartment of a four cylinder in–line diesel car engine. The definition of the design specifications and the most energetic resonance frequencies of the stochastic vibration source are identified in a first step. This is achieved using vibration data that has been measured in the engine compartment. The following section covers the optimization of the electromagnetic coupling architecture using the optimization approach presented in Chap. 3. The dependency of the output performance on additional parameters like the residual magnetic flux density of

D. Spreemann and Y. Manoli, *Electromagnetic Vibration Energy Harvesting Devices*, Springer Series in Advanced Microelectronics 35, DOI 10.1007/978-94-007-2944-5_7,

the magnet, the aspect ratio and the total construction volume are investigated. Section 7.4 addresses the design of the mechanical resonator. Transient analyses based on the measured acceleration profiles are used to find the optimal spring characteristic. In this respect nonlinear hardening– and softening springs are considered as well as pure linear springs. Consequently FEA modal and static structural analyses are used for the design of the spring element. Section 7.5 covers the performance of the assembled prototypes. Frequency response measurements have been performed and the prototypes have also been tested for excitation with measured acceleration data using a field data replication function of the lab shaker set–up. Finally, the experimental results are compared to transient analyses obtained with a full system model.

7.2 Basis for the Development

7.2.1 Underlying Vibration Characteristic

The most important condition parameter for any application oriented development of resonant vibration transducers is the available vibration. The operational environment for the development considered here is in the engine compartment of a four cylinder in–line diesel car engine. More precisely the harvester is intended to convert the vibration of fluid pipes that are connected to the engine block. Of course the ideal condition for resonant vibration conversion is a well defined vibration source with constant amplitude and frequency. However the vibration characteristic of car engines depends on the load condition and changes over time. Hence the first step in the development is to find the most energetic vibration frequencies in order to define the resonance frequency of the transducer.

To understand the speed related vibration of the car engine (acceleration) measurements have been performed under various driving conditions (city, country, and highway driving route). For this purpose two different measurement points (as shown in Fig. 7.1) have been investigated using 3–axis accelerometers. A typical result of the vibration measurements during city driving route is shown in Fig. 7.2. In the spectrogram (the magnitude of the short–time Fourier transform of the vibration signal) there are three dominant vibration frequency ranges visible (marked with the dashed lines). These frequencies are correlated to the rpm of the engine. This is due to the crankshaft drive as shown in Fig. 7.3. The rotation of the crankshaft produces oscillating and rotating inertial forces. The oscillating forces can be derived using the acceleration of the piston:

$$\ddot{x} = R \cdot (2\pi N)^2 \cdot \left(\cos\varphi + \lambda_{cp} \cos 2\varphi\right), \tag{7.1}$$

where N indicates the number of revolutions per second and λ_{cp} is the ratio of the crank arm length R_{ca} to the piston rod length l_{pr}. The mass that produce oscillating forces m_{osc} is the sum of the piston mass m_{p} and the mass of the piston rod m_{pr}. Note

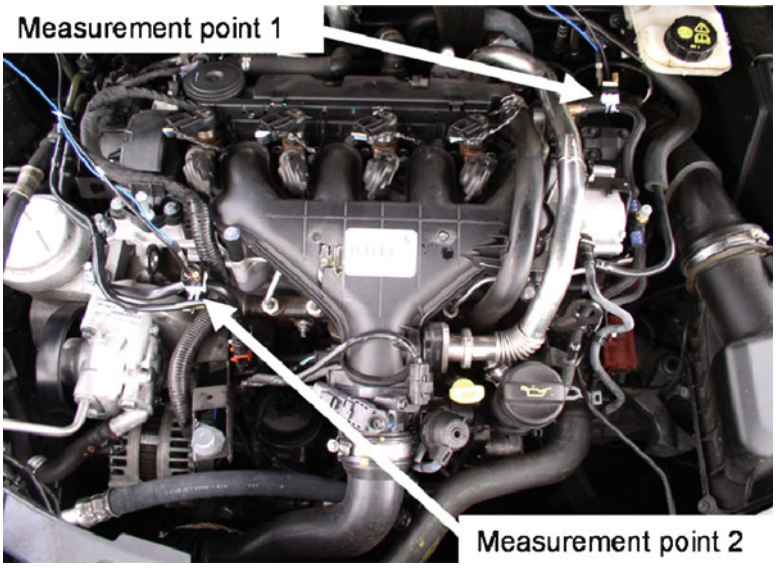

Fig. 7.1 Vibration measurements in the engine compartment of a four–cylinder in–line diesel engine

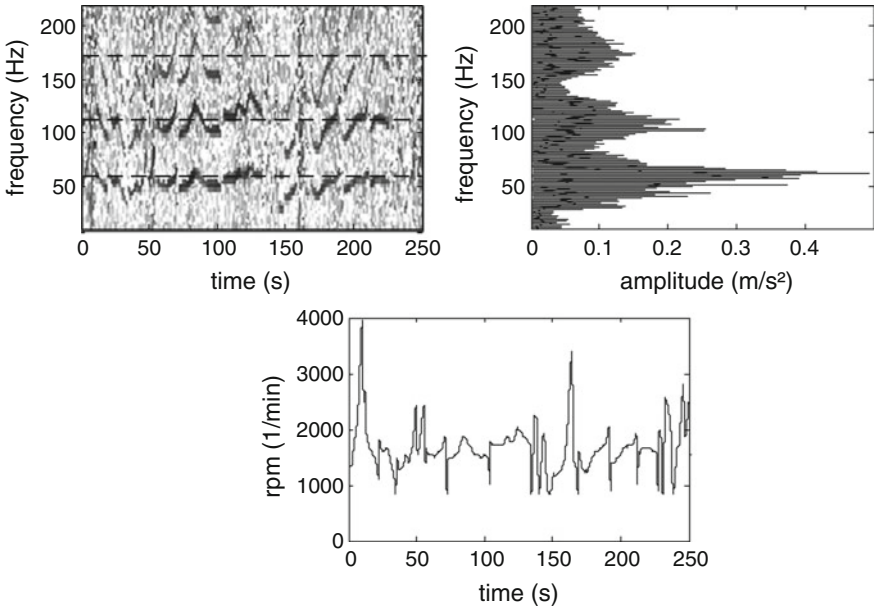

Fig. 7.2 In the spectrogram (*above left*) there are three dominant frequencies visible (*dashed horizontal lines* at about 60, 115 and 180 Hz). Consequently these frequencies are also visible in the amplitude spectrum (*above right*). The magnitude in the spectrogram is correlated to the rpm (*below*)

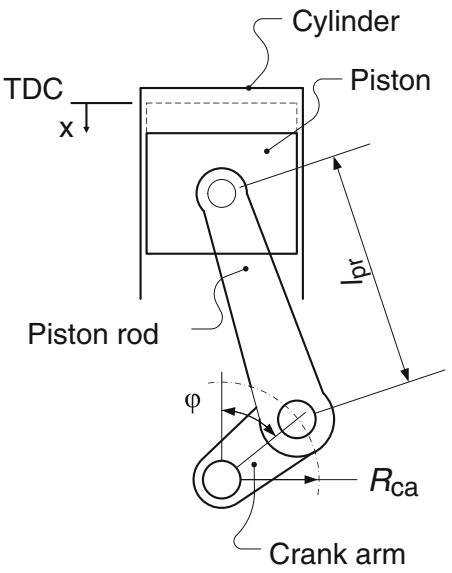

Fig. 7.3 Car engine crankshaft drive

that the crank arm is assumed to be balanced. Hence it does not produce oscillating forces in the first glance. Now the oscillating forces can be defined as:

$$F = m_{osc} \cdot \ddot{x} = \underbrace{m_{osc} \cdot R\omega^2 \cos\varphi}_{\text{first order}} + \underbrace{m_{osc} R\omega^2 \lambda_{cp} \cos 2\varphi}_{\text{second order}}, \tag{7.2}$$

where $\omega = 2\pi N$ is the angular speed. In this equation the inertia forces of the first and second order are apparent. Because in the considered four–cylinder engine the four pistons have a pairwise 180° phase shift (Cylinder $1 \rightarrow 0°$, Cylinder $2 \rightarrow 180°$, Cylinder $3 \rightarrow 360°$, Cylinder $4 \rightarrow 540°$) the first order terms will be compensated ($\cos\varphi = 1$, $\cos\varphi = -1$, respectively) in contrast to the second order terms which will be added. In general the lowest measurable engine order is obtained by dividing the number of cylinders by two. The revolution dependent frequency of the nth order can be calculated with:

$$f = \frac{rpm}{60} \cdot n, \tag{7.3}$$

where *rpm* indicates the revolution per minute. This is a simple but quite important equation because it correlates the predominant vibration frequency with the revolution per minute. The order related vibration frequencies are shown in Fig. 7.4. The frequencies of 2nd, 4th and 6th order at an rpm of about 1,600–1,700 1/min correlate with the dashed curves in the spectrogram. In order to identify the most frequent *rpm* of the total measured data (215 min of city, 92 min of country, and 16 min of highway driving route) a statistical evaluation has been performed. The result is shown in Fig. 7.5. Due to the traffic signals the idle speed is clearly present in the histogram. Altogether the most frequent rpm is between 1,600 and 1,700 1/min.

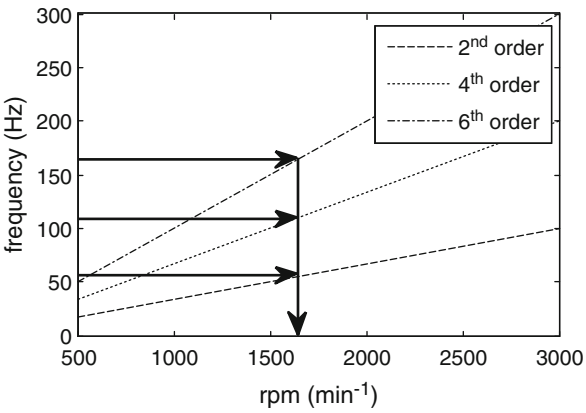

Fig. 7.4 The dominant frequencies in the spectrogram (Fig. 7.2) yield an rpm of 1,650 1/min

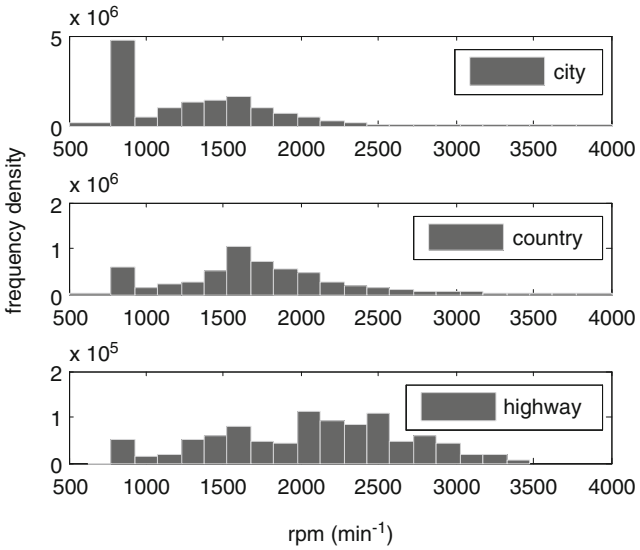

Fig. 7.5 Revolution per minute histogram for city–country–and highway driving route. In the city driving route the idle speed is dominant

According to Eq. 7.3 this corresponds to vibration frequencies of 55, 110 and 165 Hz for the 2nd, 4th and 6th order conversion, respectively. The resonance frequency of the vibration transducer should correspond to these frequencies. Beyond this fact the acceleration level at these frequencies is important to identify the most energetic resonance frequency. As indicated in Fig. 7.2 the highest acceleration level is within the 2nd engine order. The expected vibration as a mean value of the amplitudes that has been determined using discrete Fourier transform (DFT) of the measurement profiles is 2 m/s². However because the absolute value depends on the time interval where the DFT has been calculated the amplitude information is somehow delicate. It can be used as a reference value which can be significantly higher and also smaller than in reality.

Table 7.1 Specified design parameters for the optimization of the prototype electromagnetic coupling architecture

Symbol	Description	Value	Unit
Geometry			
V_{constr}	Construction volume	2.5	cm³
Z_{max}	Maximum inner displacement	1.5	mm
Magnet			
B_{r}	Residual flux density	1.1	T
ρ_{mag}	Density of magnet	7.6	g/cm³
Coil			
k_{co}	Copper fill factor	0.6	1
d_{co}	Wire diameter	40	μm
R'	Resistance per unit length	13.6	Ω/m
Other			
Y_{acc}	Excitation amplitude	2	m/s²
f	Excitation frequency	60	Hz
d_{m}	Parasitic damping	0.1	N/m/s

7.2.2 Design Specifications

As already done for the optimization and comparison of the electromagnetic coupling architectures in Sect. 3.3 it is necessary to define design specifications and initial boundary conditions before the development process can be started. In this case the boundary conditions and the specifications are imposed by the application. Table 7.1 gives a summary of the used parameters. Because the previous defined boundary conditions (refer to Table 3.2) are already based on centimeter scale vibration transducers a few parameters (like the density of the magnet, the copper fill factor, the wire diameter, the parasitic damping, ...) are still valid. However the construction volume ($h_{\text{cyl}} = 14.14$ mm, $R_0 = 7.5$ mm) has been slightly increased as well as the intended inner displacement limit. Moreover the operational excitation conditions (amplitude and frequency) have been adapted according to the findings of the previous section. In general an output power optimized design is requested. Moreover the focus of the presented prototype development lies on the conversion of the 2nd engine order (60 Hz). However two different spring elements will be designed which enables also the conversion of the 4th engine order (110 Hz) with the same prototype design.

7.3 Optimization of the Prototype Electromagnetic Coupling Architecture

7.3.1 Optimization Based on the Design Specifications

The approach for the optimization of the prototype electromagnetic coupling architecture is exactly the same as in Chap. 3. With respect to the underlying design

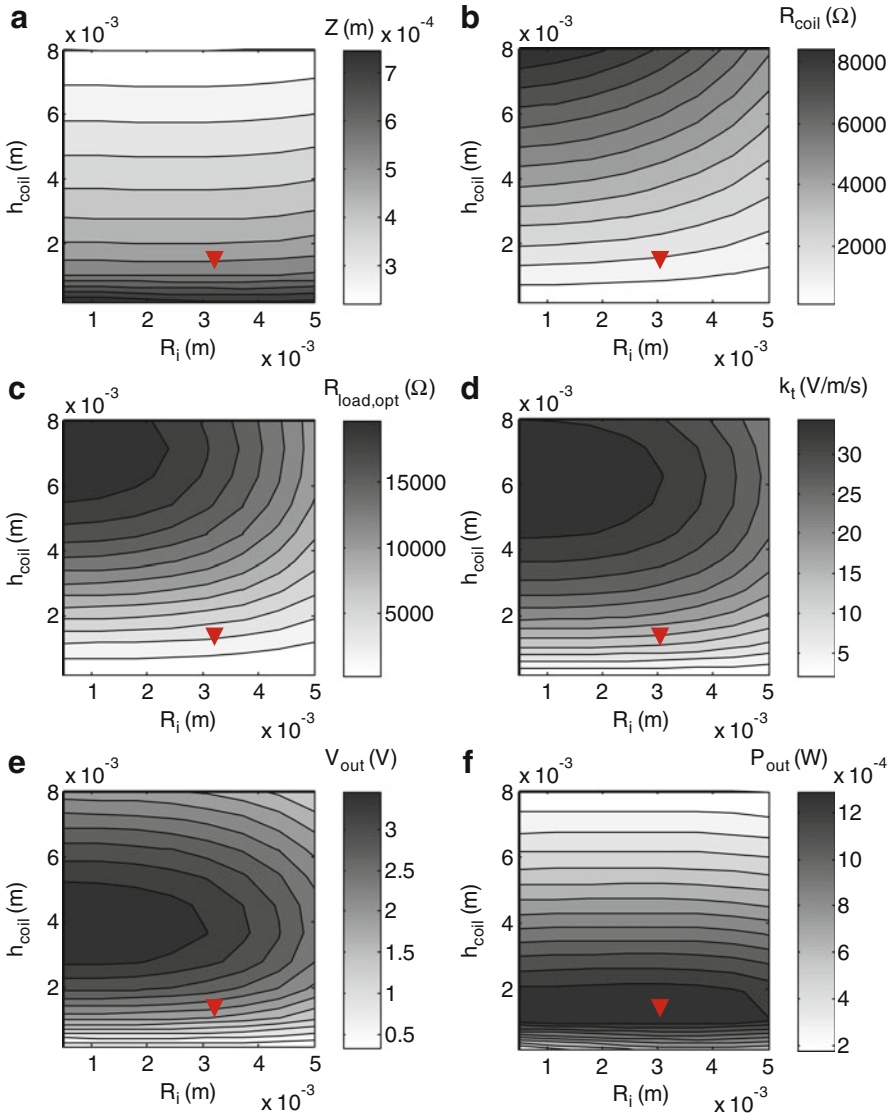

Fig. 7.6 Optimization based on the boundary conditions from application (Table 7.1). The figures shows the resulting (**a**) inner displacement amplitude, (**b**) coil resistance, (**c**) optimal load resistance for different dimensions of the coil. There are definitely different optimal dimensions for maximizing (**d**) the magnetic flux gradient, (**e**) the output voltage and (**f**) the output power

specifications and the dimensioning (as in Fig. 4.8) the results of the optimization are shown in Fig. 7.6. According to this the highest possible output power is 1.38 mW at 1.88 V for a coil with 3.07 mm inner radius and 1.70 mm height

Table 7.2 Comparison of the optimal dimensions and the dimensions that are finally used in the prototype

Symbol	Description	Optimal values (simulation)	Prototype component	Unit
R_{mag}	Outer radius of the magnet	7.50	7.50	mm
h_{mag}	Magnet height	9.57	10.00	mm
R_o	Outer radius of the coil	7.5	8.00	mm
R_i	Inner radius of the coil	3.07	3.00	mm
h_{coil}	Coil height	1.70	2.00	mm

(prototype design point). The output voltage is maximized for a coil with 0.50 mm inner radius and 3.67 mm height. With these dimensions 3.73 V can be obtained at a power level of 0.96 mW. The remaining parameter values that correspond to the optimal output power operation point can be obtained from the contour plots. Note that the resulting inner displacement amplitude for a voltage optimized design (400 μm) is smaller than for the power optimized design (560 μm). This effect is due to the volume constraint and has already been observed for the simplified model in Sect. 2.6 (Fig. 2.21). At the optimal output power point the oscillation range of the proof mass (560 μm) is about one–third of the maximal inner displacement (1.5 mm). The dimensions finally used in the prototype are based on the output power optimization results. Nevertheless they have been slightly modified in order to use standard cylindrical magnet dimensions. A comparison of the optimal values as a result of the optimization calculation and the values applied for the implementation of the prototype are given in Table 7.2.

7.3.2 Influence of Boundary Condition Parameters

In the design specifications boundary conditions have been defined which may be variable for the implementation. This section investigates the influence of these parameters on the maximum of the output power and output voltage. The first one is the aspect ratio of the cylindrical construction volume. The applied dimensions of the radius and the height yield an aspect ratio of 0.53. However, the output performance will depend on this aspect ratio. Therefore the optimization has been repeated with different aspect ratios where the maximum values of the output power and the output voltage have been recorded. The result in Fig. 7.7 shows that there are different optimal aspect ratios for the output power and the output voltage. According to this the aspect ratio used for the prototype development lies in between the optimal aspect ratio for power and voltage optimized design. Figure 7.8a–e show the results of other parameter studies where each point is the result of a separate optimization calculation. In accordance with the analytical theory the output voltage is linearly and the output power quadratically dependent on the

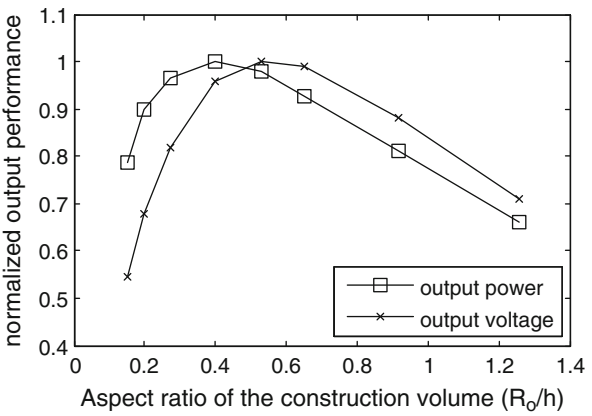

Fig. 7.7 There are different optimal aspect ratios for the construction volume where the output power and output voltage is maximal

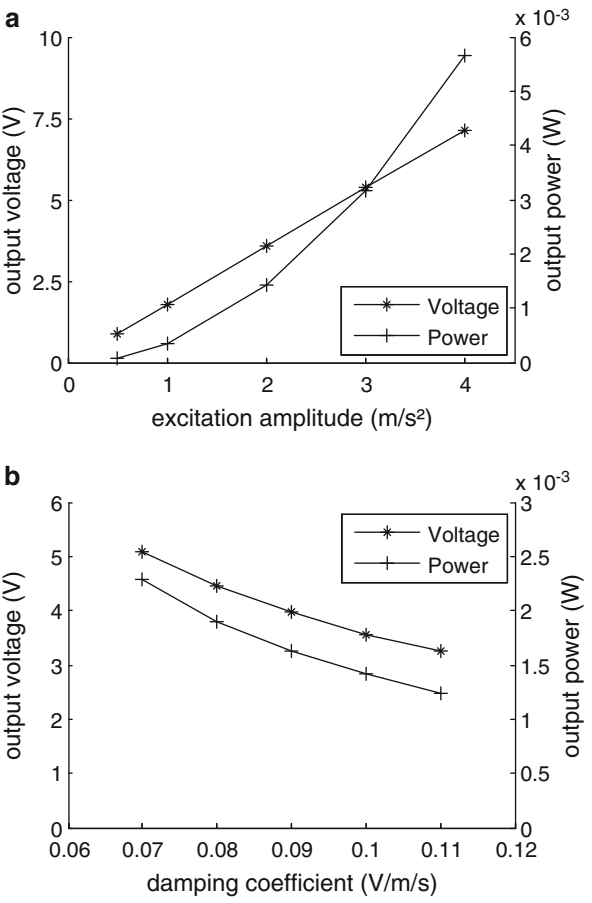

Fig. 7.8 Effect of boundary condition parameter variation on the output performance of the prototype. The diagrams show the influence of (**a**) the excitation amplitude, (**b**) the damping coefficient, (**c**) the wire diameter, (**d**) the overall construction volume and (**e**) the residual magnetic flux density

Fig. 7.8 (continued)

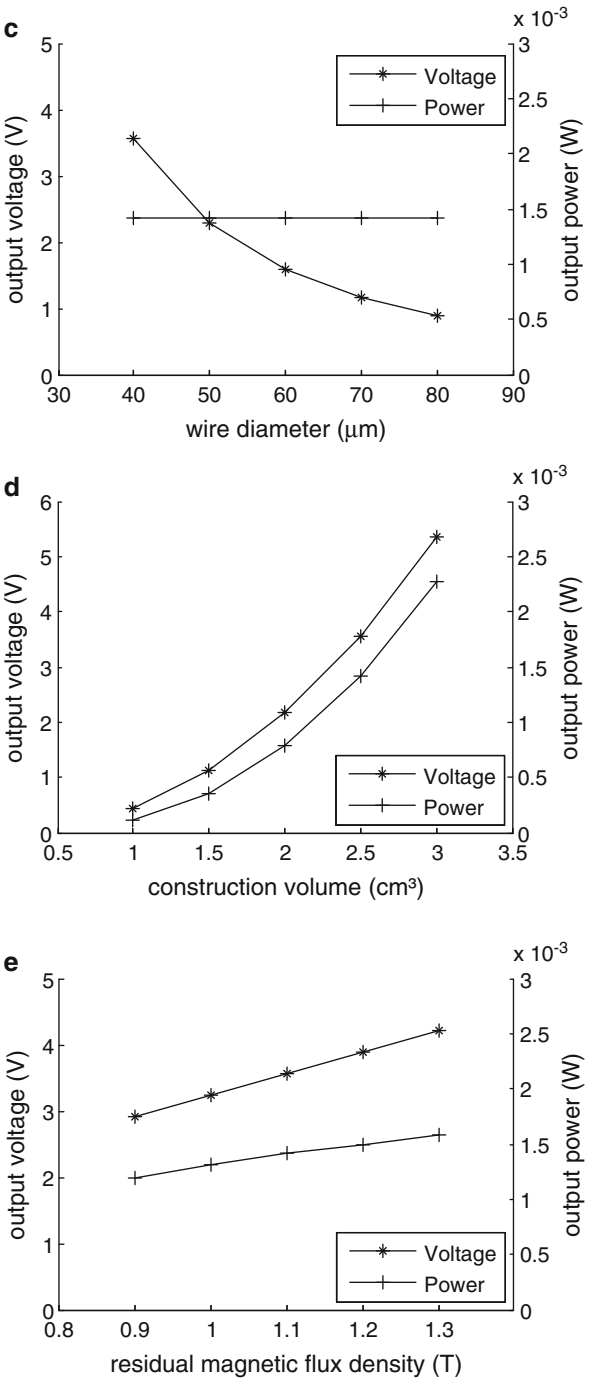

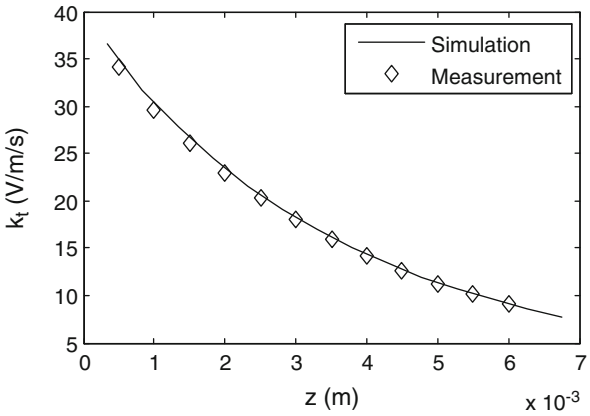

Fig. 7.9 Measured transduction factor in comparison to simulation results based on the components used in the prototype development

acceleration amplitude (a). Both the output voltage and the output power decrease with a one over x function with respect to the parasitic damping (b). Even more interesting is the influence of the wire diameter (c). Assuming a constant copper fill factor the output voltage obviously drops with larger wire diameter because the number of windings decreases. However, because the resistance decreases as well, the output power remains constant. The overall construction volume has a polynomial dependence for both the output voltage and the output power (d). Finally the influence of the residual magnetic flux density has been investigated (e). The result shows that in the typical range of NdFeB magnets the output voltage and the output power is linearly depend from the residual magnetic flux density.

7.3.3 Experimental Characterization of the Coupling Architecture

With the measurement setup that has already been used in Chap. 5 for the verification of the simulation models the transduction factor has been measured with the prototype components (magnet and coil). Based on the dimensions and the underlying winding process the coil has a resistance of 1,925 Ω and a reactance of 789 mH. The nickel plated magnet is of grade N48 with a corresponding residual magnetic flux density of 1.38 T. The result of the measurement in comparison to the simulation is shown in Fig. 7.9. The measurement is in good agreement with the simulation results. At the resting position of the magnet ($z = 1.5$ mm) the transduction factor is about 25 V/m/s. Later on in Sect. 7.5 this measured transduction factor function is implemented in a transient simulation model to simulate the prototype performance in application.

7.4 Resonator Design

7.4.1 Finding the Optimal Spring Characteristic

In Sect. 7.2.1 the most energetic resonance frequencies have been identified based on the order domain analysis. This information is sufficient to start the design process of the spring element. However, in addition it is interesting to investigate also the effect of a nonlinear spring characteristic on the output power of the resonant vibration transducer. This can be done by means of transient simulations. A schematic diagram of the underlying numerical model used for this purpose is shown in Fig. 7.10. A basic feature of this simulation model is that the dissipated power in the electromagnetic damping element can be calculated during transient simulations with the measured stochastic acceleration data as the excitation. Moreover the nonlinearity of the spring can be predefined and the oscillation range is limited (as it is for any application oriented device). The limitation of the oscillation range has been implemented by applying partially elastic collision at mechanical stoppers [2]. Some basic effects of mechanical stoppers can be explained using Fig. 7.11 where a transient oscillation is depicted for the case of unrestricted motion and several limited oscillation ranges. With respect to the unrestricted motion the limitation of the oscillation range results in a phase shift which increases with decreasing oscillation range. Moreover bouncing effects take place if the oscillation range is much smaller than the amplitude of the unrestricted motion. As steady state condition this must be avoided in application in order to reduce reliability problems.

Based on the order domain analyses results (Sect. 7.2.1) a resonance frequency range between 25 and 120 Hz is investigated using transient simulations with different spring characteristics. With the oscillation mass of the magnet (13.4 g) this corresponds to a spring rate from 315 to 7,600 N/m. Note that for the expected optimal resonance frequency of 60 Hz the spring rate is 1,900 N/m. The range of the nonlinearity is limited as well. The convention applied here is that the maximum

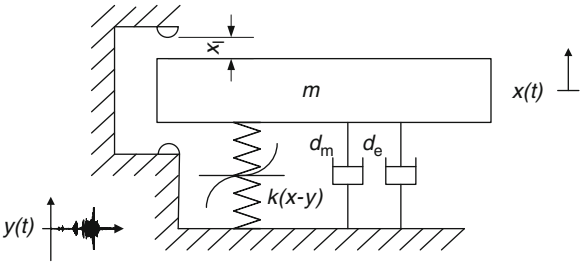

Fig. 7.10 Schematic diagram of the numerical model used for transient simulations (implemented in Matlab/Simulink®). Basic features are that the measured acceleration profile is used as the excitation, the nonlinearity of the spring can be adjusted and the oscillation range is limited by inelastic collision at mechanical stoppers

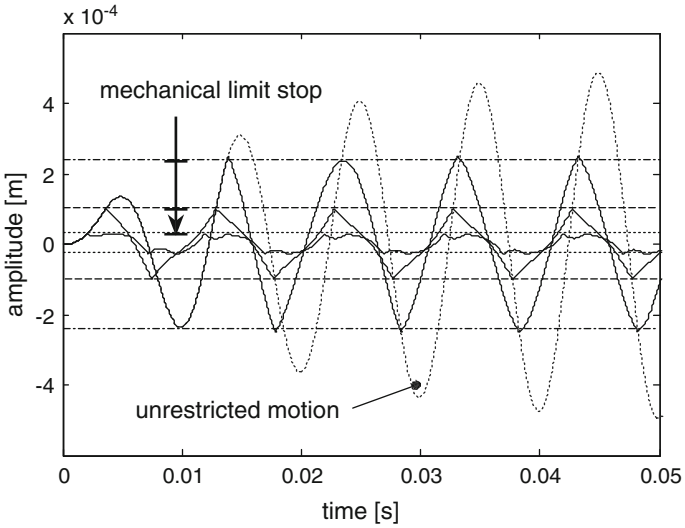

Fig. 7.11 Transient behavior of an unrestricted oscillation compared to limited oscillation ranges

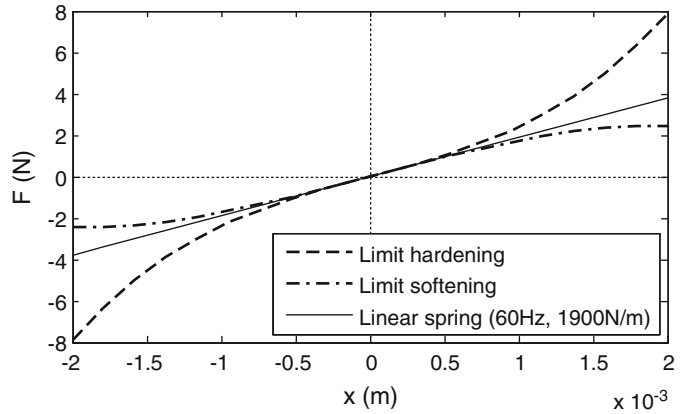

Fig. 7.12 In the simulations the nonlinearity of the spring is limited. By definition the restoring force of the hardening spring at 2 mm inner displacement is twice as much as for the linear spring and the softening spring must be monotonically increasing

restoring force of hardening springs at 2 mm internal displacement is twice the amplitude as for the linear spring and the softening spring must be monotonically increasing. For the 60 Hz respectively 1,900 N/m spring this limitation is shown in Fig. 7.12.

The simulation result for a city driving route and a displacement limit of $x_l = 1.5$ mm is used to explain some important characteristics (Fig. 7.13). Note that for clearness the linear spring rate k on the x–axis has been converted into the

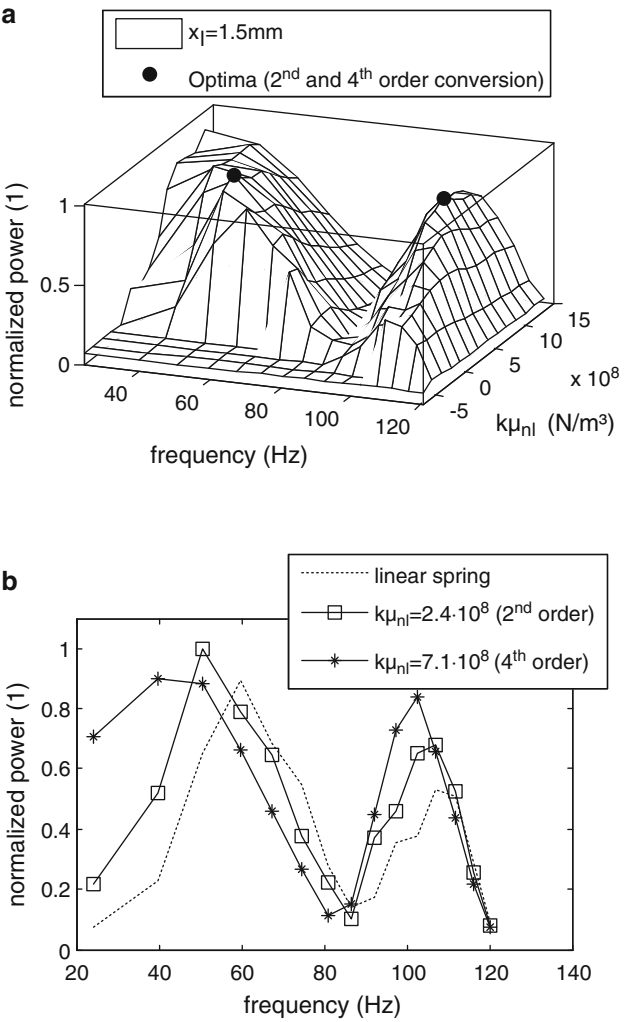

Fig. 7.13 (**a**) Normalized output power for an example (city driving route) excitation and different spring characteristics. (**b**) The output power can be increased by 10% for the 2nd and by 25% for the 4th order conversion using nonlinear hardening springs. (**c**) and (**d**) Optimal spring characteristic in comparison to the best linear springs

frequency using $f = \sqrt{k/m}/2\pi$. Moreover the output power that corresponds to spring characteristics beyond the bounds is set to zero. First of all the 2nd and 4th engine order are clearly visible in the output power surface (Fig. 7.13a). For pure linear springs ($k\mu_{\mathrm{nl}} = 0$) the highest output power is obtained at a frequency that correspond to the second order conversion. For both frequencies (2nd and 4th order) the output power decreases for softening springs ($k\mu_{\mathrm{nl}} < 0$) but increases for hardening springs ($k\mu_{\mathrm{nl}} > 0$). With respect to the 2nd order conversion this effect

Fig. 7.13 (continued)

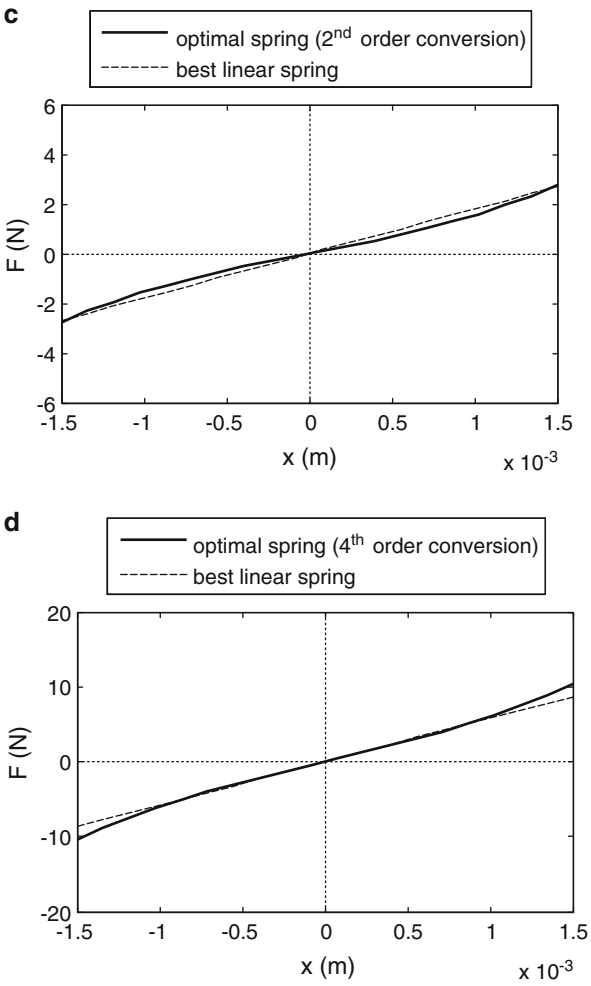

is marginal in contrast to the 4th order conversion. In Fig. 7.13b the output power for a linear spring and for the nonlinearity that corresponds to the optima of the 2nd and 4th order is plotted. This result shows that for pure linear springs the output power is 40% higher for the 2nd order conversion with respect to the 4th order conversion. Using nonlinear hardening springs the output power can further be increased by about 10% for the 2nd order conversion and by about 25% for the 4th order conversion. Note that in this example the output power for 4th order conversion with an optimized hardening spring is almost the same as for the 2nd order conversion with a linear spring. The spring characteristic corresponding to the optima in comparison to the best linear springs are given in Fig. 7.13c, d.

So far the inner displacement limit x_1 was used in the simulation. However, the optimal spring characteristic depends on the value of x_1. To show the influence

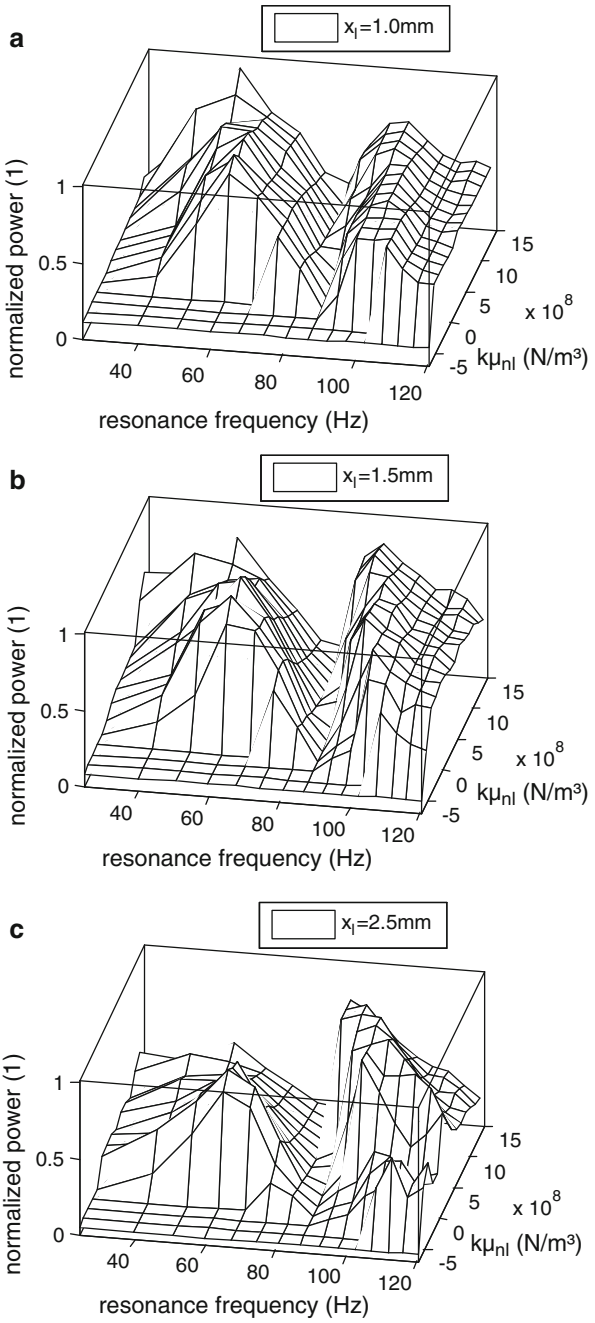

Fig. 7.14 Normalized output power for different spring characteristics and inner displacement limits. The 4th order conversion increases with the inner displacement limit. Finally at 2.5 mm inner displacement the 4th order conversion become more efficient than the 2nd order conversion

simulation results of a country driving route at different inner displacement limits are shown in Fig. 7.14. Again the 2nd and 4th order are clearly distinct. The output power of the 2nd order conversion at $x_l = 1.0$ mm is about 30% higher than for the

4th order conversion. At this point the use of nonlinear springs is not advantageous because the output power can only be increased marginally (about 5% for 2nd order conversion and 2% for 4th order conversion). For $x_l = 1.5$ mm the efficiency of both orders are somehow equivalent and even though the benefit is still marginal nonlinear hardening springs are capable of maximizing the output power of the 4th order conversion. For further increase of $x_l = 2.5$ mm the 4th order conversion becomes more effective (about 20%) than the 2nd order conversion. However in the simulation it is easy to apply an arbitrary inner displacement limit. In the application this value is always limited by the fatigue limit of the spring material. Altogether the investigations presented in this section lead to the conclusion that nonlinear hardening springs are capable to maximize the output power especially for the 4th order conversion and $x_l \geq 1.5$ mm. Nevertheless the benefit is not significant and the realization of predefined nonlinear springs with high oscillation ranges evokes further challenges especially for the stiff system required for the 4th order conversion. For the development of the presented prototype it is still reasonable to focus on the 2nd order conversion with a linear system. Nevertheless Appendix C introduces an approach for the realization of predefined nonlinear hardening springs for vibration transducers based on cantilever beams.

As a final conclusion it must be pointed out that even though nonlinear springs have the potential to increase the converted output power in resonant vibration transducers there is no general advantage. To determine the capability the underlying vibration source, the desired resonance frequency and the inner displacement limit have to be taken into account and numerical transient simulations should be involved into the design process.

7.4.2 FEA Based Design of the Spring Element

In vibration transducers the resonator is primarily defined by the spring element together with the oscillating mass. The resonator assembly used here is shown in Fig. 7.15. The cylindrical magnet is placed in a pot like support (casting component). Both components create the oscillating mass which is connected to a planar spring element using ultrasonic riveting. The most essential requirements for the spring element are to provide the stiffness which yields the desired resonance frequency and to provide a preferably high oscillation amplitude without causing fatigue problems. FEA based modal– and static structural analyses have been used to achieve the correct stiffness and to determine the maximum allowable deflection. The solid model of the planar spring element (Fig. 7.16a) consists essentially of three spiral beams, a central bore hole for the magnet support and outer bore holes to provide the casting of the spring element in the housing. In the defeatured model for FEA calculations (Fig. 7.16b) the parameters height, width, length and the inclination of the beam elements define the stiffness of the CuSn6 spring element. These parameters need to be adjusted in order to achieve the desired resonance frequency. The most important material parameter is the

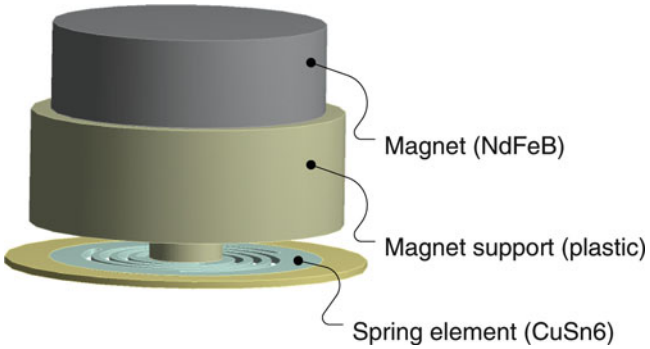

Fig. 7.15 Considered resonator assembly

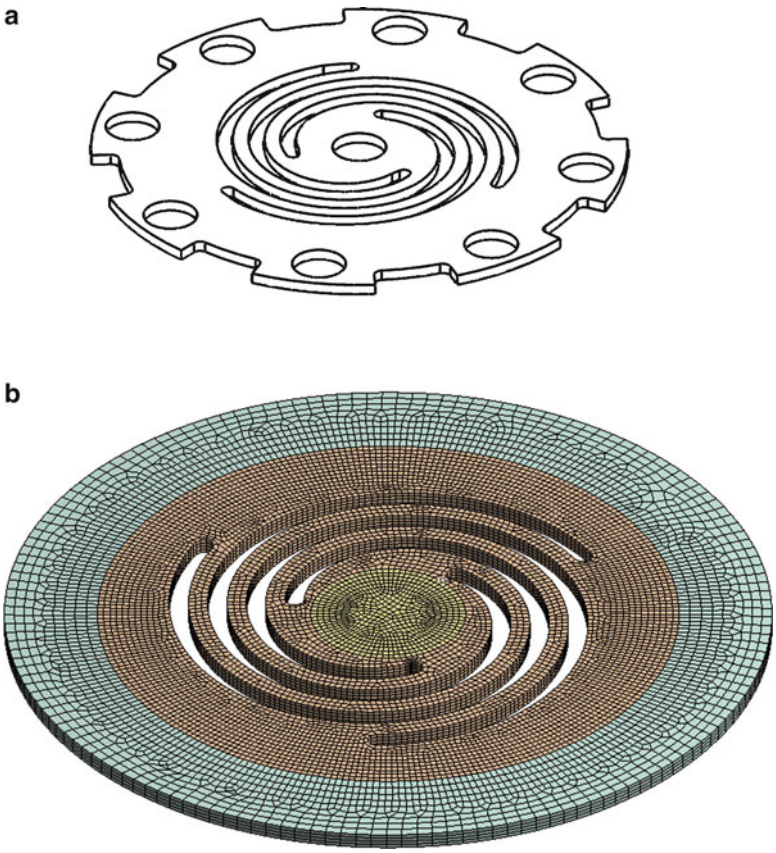

Fig. 7.16 (**a**) Spring element with central hole for the magnet support and with outer holes to provide the mould process. (**b**) Defeatured and meshed solid model of the spring element used for FEA simulations

Table 7.3 Most important material parameters of the spring material CuSn6 R550 (UNS C51900)

Symbol	Description	Value	Unit
ρ_{CuSn6}	density	8.82	g/cm³
E	Young's modulus (at 20°C/annealed)	118	kN/mm²
S_U	Tensile strength	550–650	N/mm²
$R_{p0.2}$	Yield strength	≥500	N/mm²

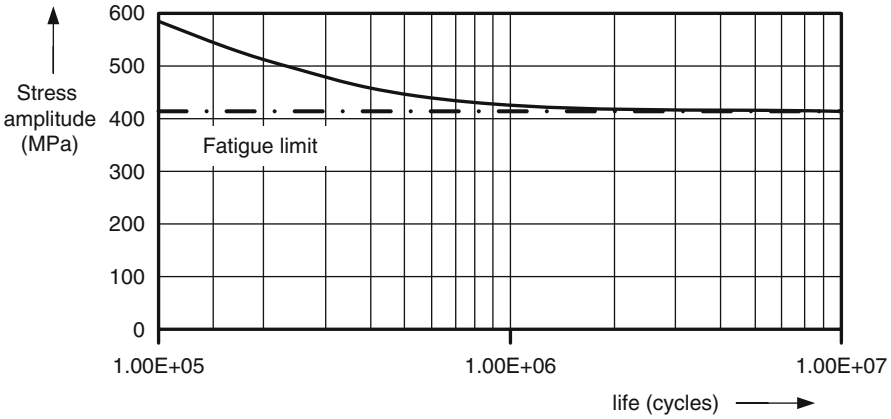

Fig. 7.17 Wöhler curve of CuSn6 R550 (UNS C51900) [10]

Young's modulus. Further material parameters are summarized in Table 7.3. To operate below the fatigue limit of the material the maximum cyclic stress amplitude (at maximum displacement) has to be well below the Yield strength. The exact material performance is characterized in the Wöhler curve (Fig. 7.17). Based on this curve the maximum stress amplitude has to be smaller than about 410 MPa. Note that the continuous operation at 60 Hz for about half a year already results in about 10^9 cycles. Modal analyses have been performed to find a parameter set of the beam structure that yields the desired resonance frequencies. The first three modes are depicted in Fig. 7.18. Mode one and two are unwanted rotary oscillations whereas mode three is a pure axial movement which is desired for the single degree of freedom energy conversion. In principle these modes are the same for the 2nd and 4th order conversion prototype. The von–Mises stress in the spring element at the 3rd mode is shown in Fig. 7.19. The highest stress amplitudes result where the beam elements merge into the outer ring (detail view). This is the region where fatigue problems will appear first. The results of the simulated resonance frequencies beside the maximum displacement amplitudes for both prototypes are summarized in Table 7.4. At this point it is apparent that especially for the 4th order conversion prototype the system is limited by the fatigue limitation of the spring element even though the output power could further be increased for higher inner displacement limits.

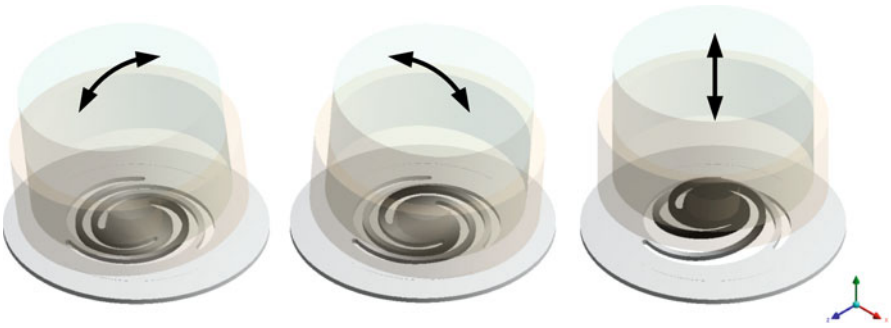

Fig. 7.18 First three modes of the resonator system. The linear oscillation of the 3rd mode is used for energy conversion

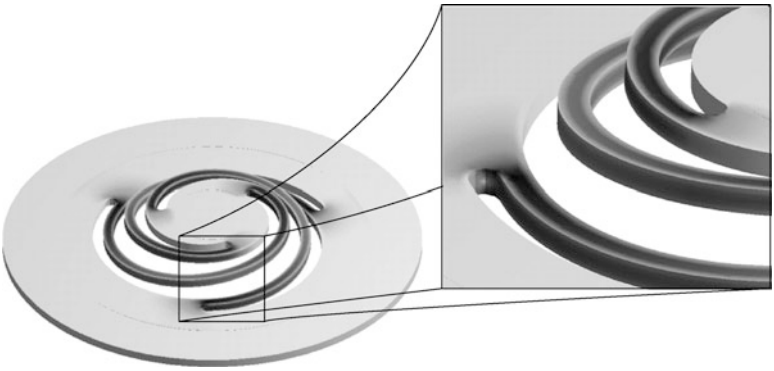

Fig. 7.19 Equivalent (von–Mises) stress in the spring element. The highest stress level results where the beam merges into the outer ring

Table 7.4 Eigenfrequencies and maximum amplitudes for operation below the fatigue limit

Spring element	1st mode (Hz)	2nd mode (Hz)	3rd mode (Hz)	Maximum amplitude (mm)
2nd order conversion	27.63	27.64	59.52	1.0
4th order conversion	43.27	43.95	102.09	0.5

7.4.3 Experimental Characterization of the Spring Element

The spring elements are manufactured using laser precision cutting (Fig. 7.20). A picture of a manufactured spring element before and after the mould process in the casing is shown in Fig. 7.21. In static measurements the force–deflection relation of ten samples of the manufactured spring elements has been measured. The results are shown in Fig. 7.22. The mean value of the spring constant for 2nd order conversion is 1,650 N/m and for the 4th order conversion 5,290 N/m. Both

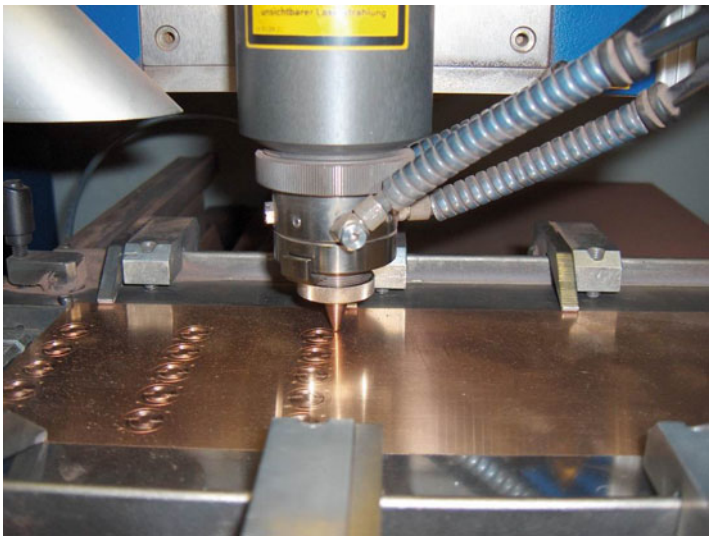

Fig. 7.20 Laser precision cutting of the CuSn6 spring element

spring types have practically a pure linear behavior in the denoted oscillation range. The deviation of the spring constant caused by manufacturing tolerances yields a resonance frequency shift in the range of ± 1 Hz. This is quite reasonable for the considered application. To proof the fatigue limitation the spring has further been overstressed by exceeding the specified oscillation range. As predicted in the FEA results fatigue problems appears at the maximum stress point (Fig. 7.23). In the prototypes this is avoided by adjusting the inner displacement limit according to the FEA results of the last section.

7.5 Prototype Assembling and Performance

The last two sections cover the design and optimization of the most basic components of the resonant vibration transducer prototype. These are namely the magnet, the coil and the spring element. The assembly of the complete prototype is based on a standard injection moulding process with an aluminium prototype casting–mould. The used material is polyamide PA 12. The design is shown in Fig. 7.24. With the spring element moulded in the casing the order of assembly is as follows:

1. First the magnet is glued into the magnet support.
2. These two components are connected to the spring element using ultrasonic riveting.
3. The coil is glued on the assembled PCB.

Fig. 7.21 CuSn6 spring element (**a**) before and (**b**) after the mould process. In the middle the rivet head of the magnet support is visible. The spring element in (**a**) is for 2nd order conversion (smaller beam width) and in (**b**) for 4th order conversion prototype

4. The PCB (together with the coil), the casing (with the cast–in spring and the magnet) and the spacer can afterwards be inserted into the cap.
5. Finally the base with the fixing clip is glued together with the cap. Alternatively ultrasonic welding can be used.

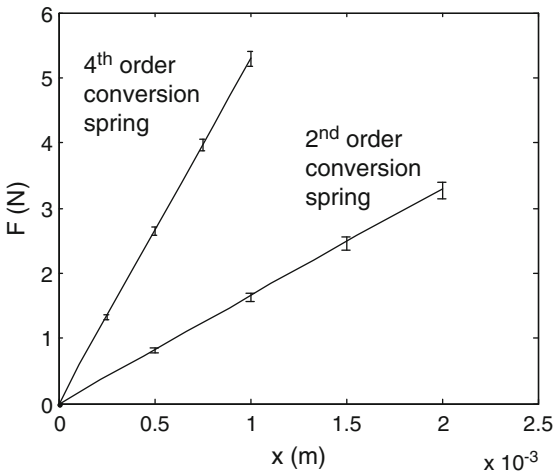

Fig. 7.22 Measured characteristic of the 2nd order and the 4th order conversion spring

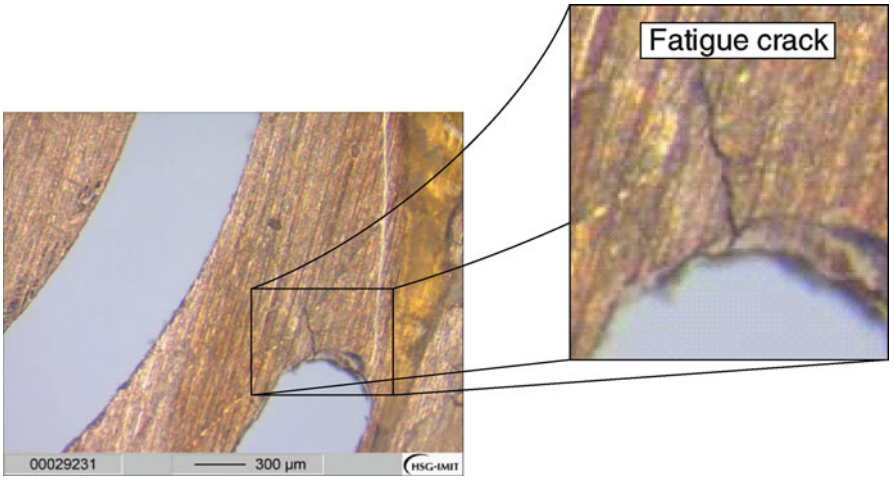

Fig. 7.23 In accordance with the FEA simulation fatigue problems appears first at the maximum stress point

Based on these steps a series of 2nd order and 4th order conversion prototypes (the only difference between the prototypes is the spring element) have been fabricated and tested. The limitation of the oscillation range is defined by the rivet head (lower bound) and the magnet support together with the spacer (upper bound). However the rivet head could not be realized as flat as expected which finally reduces the oscillation range to about 0.4 mm. As a first experimental characterization the frequency response of the prototypes mounted on a shaker setup has been measured. The results at different excitation amplitudes for the 2nd order conversion prototype are shown in Fig. 7.25 and for the 4th order

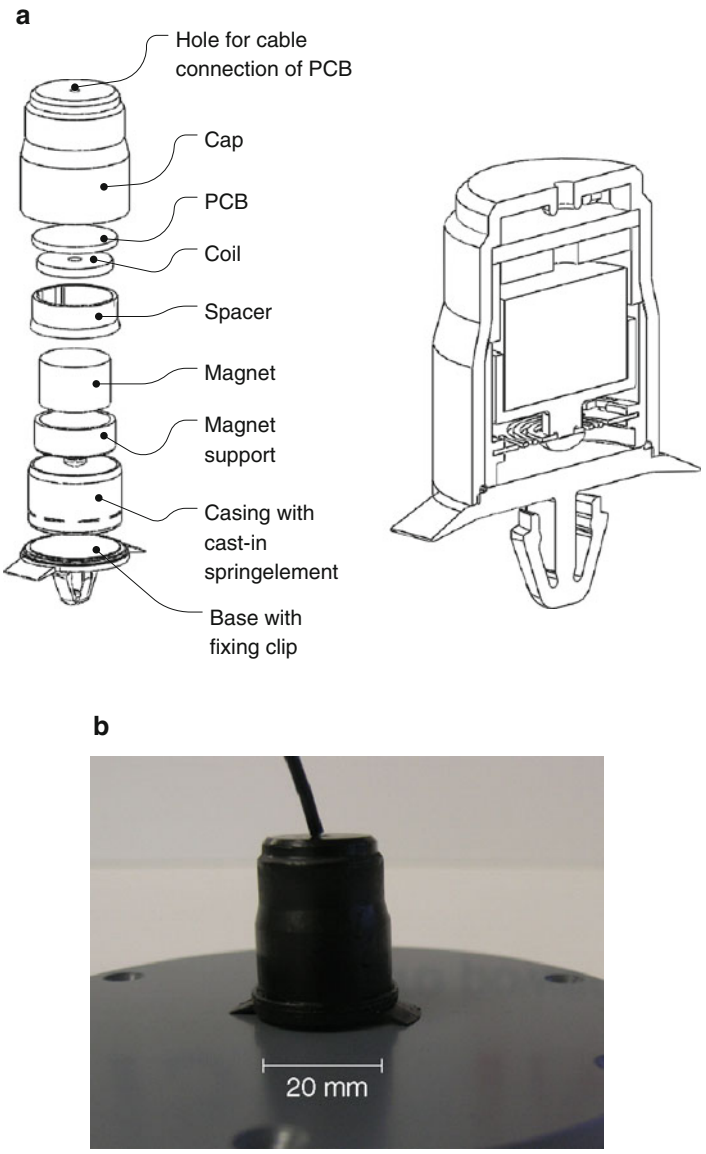

Fig. 7.24 (**a**) Exploded and sectional view of the prototype. (**b**) Photograph of an assembled device

conversion prototype in Fig. 7.26. The measured resonance frequencies (55.90 Hz for 2nd– and 107.20 for 4th order conversion prototype) are in good agreement with the prediction from the FEA (6% and 5% deviation). Note that at the specified excitation level (refer to Table 7.1) the voltage level is in the range of 3 V which

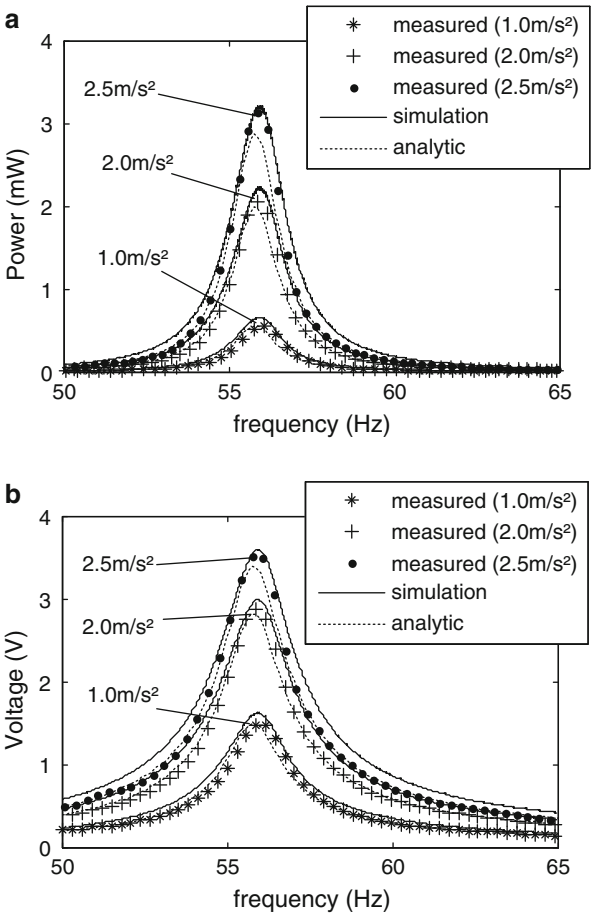

Fig. 7.25 Measured output voltage (**a**) and output power (**b**) of the 2nd order conversion prototype at different excitation amplitudes and a resistive load of 4 kΩ. The measured values are compared to results obtained from transient simulation and to analytically calculated curves

is comfortable for rectification. The power is greater than 2 mW. The simulated curves have been obtained using transient simulations. For this reason the model already used for the design of the resonator (Fig. 7.10) has been enhanced such that the electrical load circuit (pure resistive load) can be included. To perform the transient simulations the parasitic damping coefficient d_m must be specified in the first step. With the data of the measured (voltage) frequency response the combined electromagnetic and parasitic damping coefficient $(d_\mathrm{e} + d_\mathrm{m})$ can easily be calculated with (Fig. 7.27):

$$Q = \frac{\omega_0}{\Delta\omega} \longrightarrow d = d_\mathrm{e} + d_m = \frac{m\omega_0}{Q} = m\Delta\omega. \tag{7.4}$$

Q is the quality factor, ω_0 the angular resonance frequency and $\Delta\omega$ the angular bandwidth (at −3 db). The pure parasitic damping coefficient can be obtained by

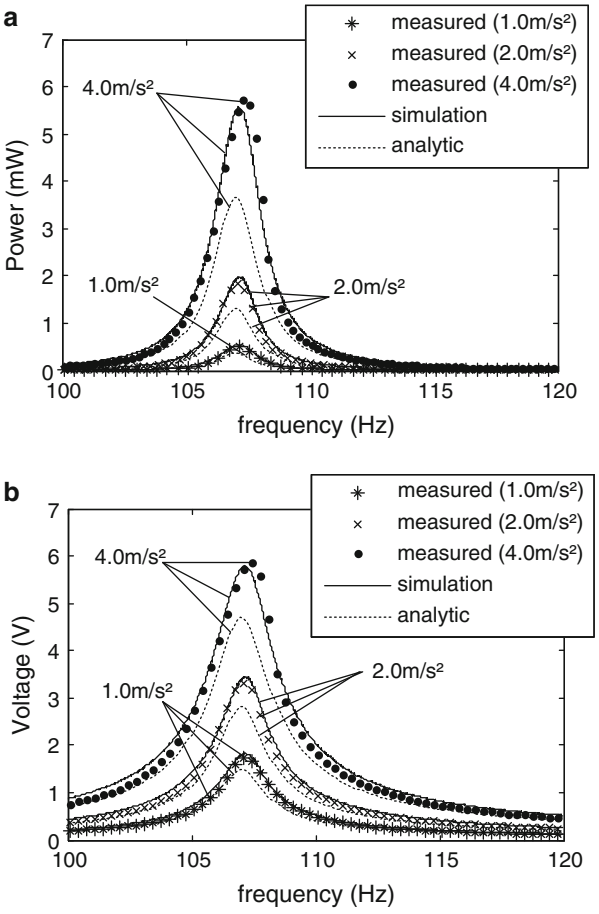

Fig. 7.26 Measured output voltage (**a**) and output power (**b**) of the 4th order conversion prototype at different excitation amplitudes and a resistive load of 6 kΩ. The measured values are compared to results obtained from transient simulation and to analytically calculated curves

calculation of d_e using (2.32). Note that due to eddy currents it is not feasible to determine the parasitic damping directly from the open circuit voltage frequency response.

Beside the damping coefficients the measured curve of the transduction factor (Fig. 7.9) has been implemented in the transient simulation model using a lookup table. As in reality this results in a nonlinear electromagnetic damping because the transduction factor depends on the position of the oscillating magnet. With the measured parameters included in the transient simulation model the simulation results are in very good agreement with the measured frequency response data and thus the transient simulation model is verified. In the next step it is adequate to assess the prototype performance for the stochastic excitation in the actual application.

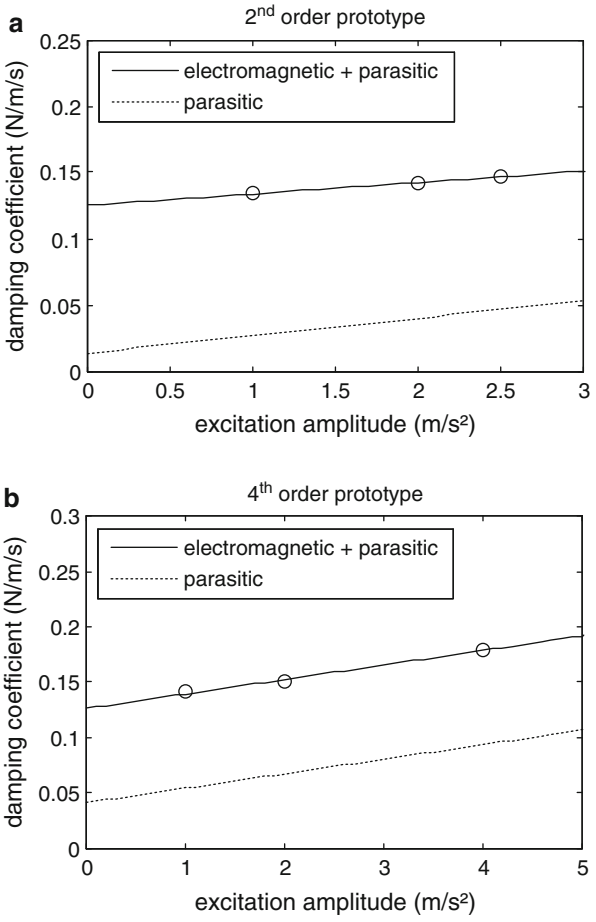

Fig. 7.27 Damping coefficient of (**a**) prototype for 2nd – and (**b**) prototype for 4th order conversion. The damping coefficient depends linearly on the excitation amplitude respectively the inner displacement

In the simulation this has been done by replacing the harmonic frequency sweep function with the measured acceleration data. Typical results of the output voltage and output power at a 4 kΩ load resistance for a city driving route is shown in Fig. 7.28 and for a country driving route in Fig. 7.29. The measured values (red transparent) have been obtained with a 2nd order prototype and a field data replication using a shaker setup. Because the control unit needs some time until the shaker acceleration matches the field data acceleration the first 30 s are truncated in the measurement. Again the results of the measurement and simulation are in very good agreement. Qualitatively the high energy sequences (>1 V) in the city driving routes are smaller than in the country driving route and there are periods (up to tens of seconds) where the generated power is not easily applicable (<1 V). The mean value of the output power for all city driving routes is about 82 μW with a standard deviation of 25 μW. By increasing the inner displacement limit to the specified value of $x_l = 1.5$ mm the mean power increases to 176 μW. For country driving routes the

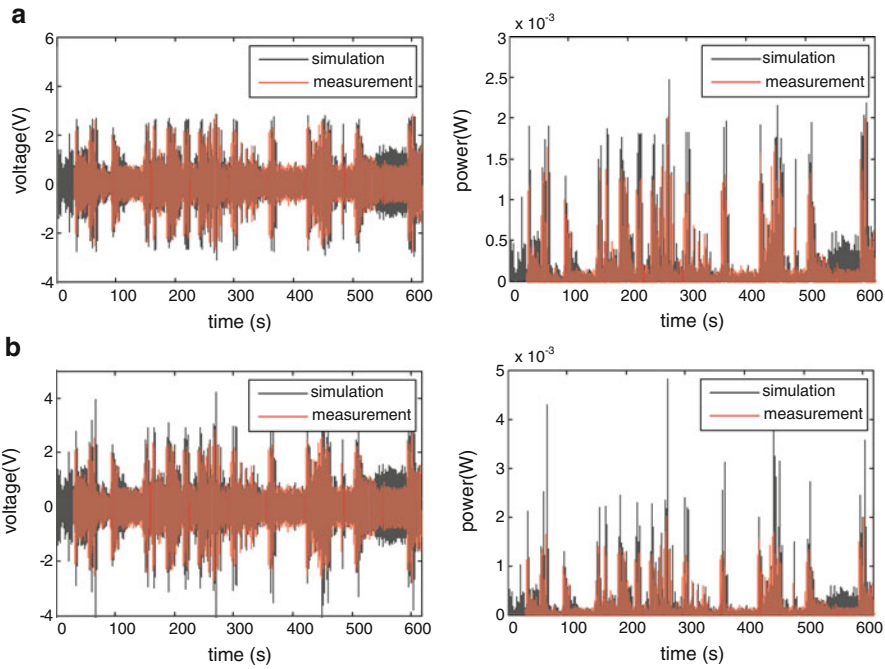

Fig. 7.28 Measured and simulated voltage and power for excitation with a city driving route vibration profile. In (**a**) the inner displacement limit in the simulation is set to 0.4 mm and in (**b**) to 1.5 mm

mean value of the output power is 143 μW with a standard deviation of 47 μW. By increasing the inner displacement limit to the specified value the mean power can be increased to 321 μW. The output power with the 4th order conversion prototype is significantly smaller (about 50%). The measured output power for city driving routes is 45 ± 25 μW and for country driving routes 98 ± 29 μW.

7.6 Conclusions

To show how the optimization approach presented in Chap. 3 can be integrated into the design flow of resonant vibration transducers this chapter described an application oriented development of an electromagnetic vibration transducer. As a basis for the design the underlying vibration source (four cylinder in–line diesel engine) was characterised in the first step. Using the order domain analyses together with statistical evaluation of measured *rpm* and DFT calculations the most energetic resonance frequency was identified (60 Hz). In the next step the electromagnetic coupling architecture has been dimensioned based on specified design parameters (Table 7.1). The investigation of design parameter variations on

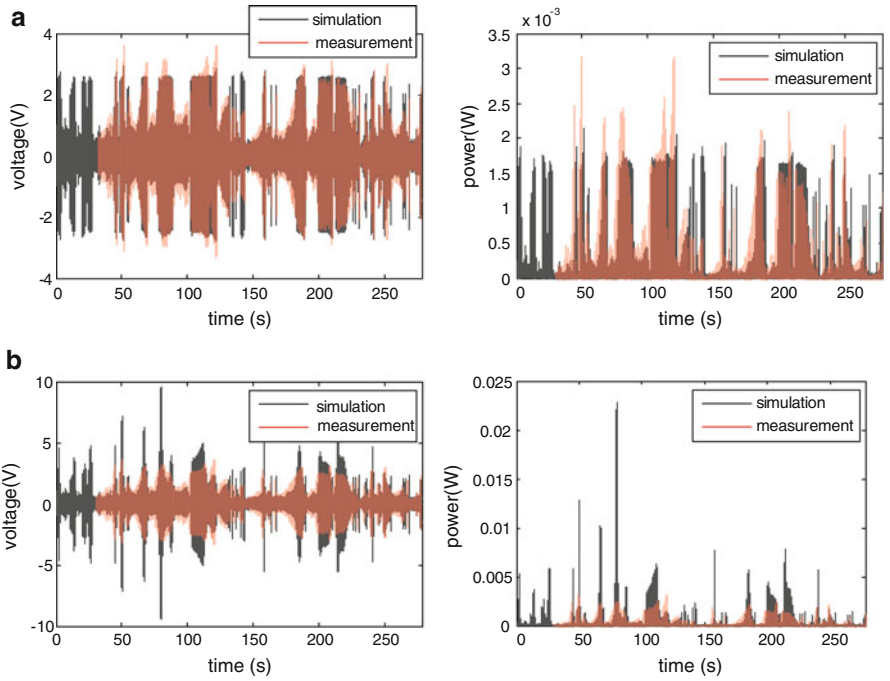

Fig. 7.29 Measured and simulated voltage and power for excitation with a country driving route vibration profile. In (**a**) the inner displacement limit in the simulation is set to 0.4 mm and in (**b**) to 1.5 mm

the output performance reveals further important dependencies. One of them is that there exists an optimal aspect ratio of the construction volume. This aspect ratio is different for voltage and power generation.

Afterwards the optimal spring characteristic has been defined using transient simulations with the measured acceleration data as excitation. It could be shown that the 2nd order conversion is more effective than the 4th order conversion. Moreover nonlinear hardening springs have the potential to increase the output power. However, to determine the capability the underlying stochastic vibration source, the desired resonance frequency and the inner displacement limit have to be taken into account. Based on these results static mechanic and modal FEA calculations have been used to design a planar spring element which was manufactured from CuSn6 using laser precision cutting. In order to avoid fatigue problems the inner displacement limit has been reduced such that the maximum stress in the spring is smaller than 410 MPa. This guarantees that the spring survives at least 10^7 cycles. The overloading of a spring element evokes crack initiation. The point where this fatigue problem emerges is in accordance with the FEA calculations.

Consequently prototype vibration transducers for 2nd and 4th order conversion have been assembled based on a standard injection moulding process.

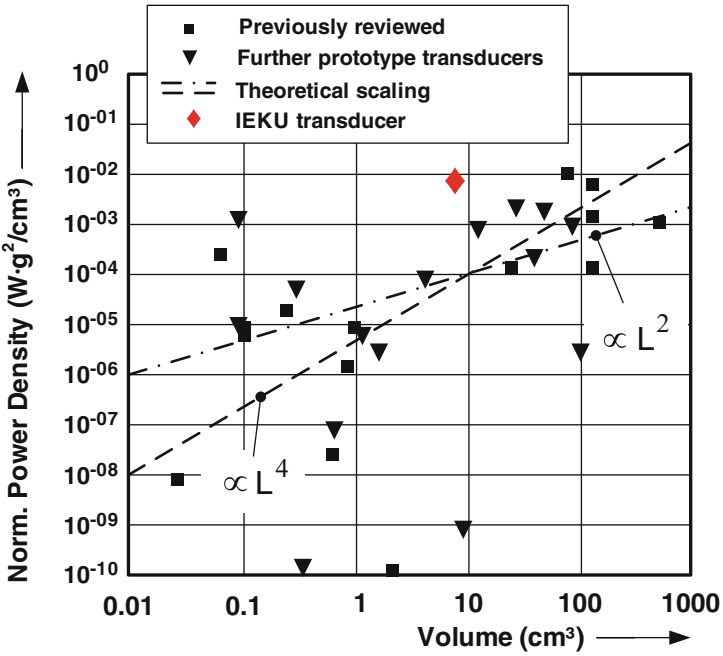

Fig. 7.30 Previously reviewed vibration transducer prototypes in [27] and transducers reviewed in this book. This figure is identical with Fig. 1.6. However the normalized power density of the prototypes developed in this book based on the presented optimization approach has been added

The prototypes have first been qualified on a lab shaker set–up with harmonic frequency sweeps as excitation. The measurement results shows that the power density of the prototype transducers developed in this book based on the presented optimization approach are among the best of the reviewed transducers in [27] and in Sect. 1.2 (Fig. 7.30). With the measured data the parasitic damping factor could be determined. Together with the measured transduction factor function the measured damping factors has been included into an enhanced transient model. Finally the simulated frequency response values are in good agreement with the measured curves. Afterwards the field data replication function of the shaker set–up has been used to assess the output performance of the transducers for the stochastic vibration as in the application. Also in this case the transient simulation model is capable to predict the measured values. In the application this enables the prediction of expected maximum values, mean values or the time periods which need to be overcome. As expected in application the 2nd order prototype definitely performs better than the 4th order prototype in the application.